Solid Earth Discuss., 5, 2005–2042, 2013
www.solid-earth-discuss.net/5/2005/2013/
doi:10.5194/sed-5-2005-2013

Solid Earth
Discussions
Open Access

The ring-shaped thermal field of Stefanos crater, Nisyros Island: a conceptual model

M. Pantaleo and T. R. Walter

Department 2, Physics of the Earth, Helmholtz-Centre Potsdam, GFZ German Research Centre for Geoscience, Potsdam 14473, Germany

Received: 24 October 2013 – Accepted: 31 October 2013 – Published: 14 November 2013

Correspondence to: M. Pantaleo (pantal@gfz-potsdam.de)

Published by Copernicus Publications on behalf of the European Geosciences Union.

Title Page
Abstract | Introduction
Conclusions | References
Tables | Figures
◀| |▶
◀ ▶
Back | Close
Full Screen / Esc
Printer-friendly Version
Interactive Discussion

Abstract

Fumarole fields related to hydrothermal processes release the heat of the underground through permeable pathways. Thermal changes, therefore, are likely to depend also on the variation of these pathways. As these paths may affect or even control the temperature field at the surface, their understanding is relevant to applied and basic science alike. A common difficulty, however, in surface temperature field studies at active volcanoes is that the parameters controlling the ascending routes of fluids are poorly constrained in general. Here we analyze the crater of Stefanos, Nisyros (Greece), and highlight complexities in the spatial pattern of the fumarole field related to permeability conditions. There may be different explanations for the observed permeability changes, such as structural control, lithology, weathering, and heterogeneous sediment accumulation and erosion. We combine high resolution infrared mosaics and grain-size analysis of soils, aiming to elaborate parameters controlling the appearance of the fumarole field. We find a ring-shaped thermal field located within the explosion crater, which is dependent on contrasts of the soil granulometry and volcanotectonic history. We develop a conceptual model of how the ring-shaped thermal field has formed at the Stefanos crater and similarly at other volcanic edifices, highlighting the importance of local permeability contrast that may increase or decrease the thermal fluid flux.

1 Introduction

Thermal anomalies at volcanic areas may be detected before, during and long after eruptions, allowing assessment of precursors, of fluid flux and degassing intensity levels, and the volcanic heat discharge at the surface (Sekioka and Yuhara, 1974; Stevenson, 1993). Besides the magmatic/hydrothermal source itself, different factors may affect the expression and intensity of fumaroles, e.g. the stress field, the presence of faults and fractures, and the lithology (Mongillo and Wood, 1995; Finizola et al., 2003; Revil et al., 2008; Schöpa et al., 2011; Peltier et al., 2012). The release of hot fluids at the surface can be detected by direct and remote measurements (Bukumirovic et al., 1997; Harris and Maciejewski, 2000; Chiodini et al., 2007) and by hand-held infrared cameras (Chiodini et al., 2007; Harris et al., 2009). However the question of how the thermal expression at a volcanic crater is affected by permeability complexities remains to be studied, especially in terms of edifice morphology, and of the tectonic and of evolutive stage. Few case studies have investigated this topic (Mongillo and Wood, 1995; Schöpa et al., 2011; Peltier et al., 2012), highlighting the entanglement between the parameters that control permeability. Mongillo et al. (1995) showed at White Island, New Zealand, that the structures control the site permeability at edifice scale, whereas the lithology has a local influence on it. Schopa et al. (2011) indicated that at Vulcano Island, Italy, the topography-induced stress field focuses the permeable pathways toward the morphological crests, where the lithology and the shallow structures finally become dominant. Peltier et al. (2012) suggested that at Yasur-Yenkahe complex, Vanuatu, the stratigraphic conditions dictate the permeability setting together with structures which intercept the permeable layers. The reconnaissance of the permeability background becomes relevant to decipher the temporal and spatial variability of thermal fields as it also relates to unrest. Faults, fractures and lithologies, in particular, control the permeability of the rock masses (Curewitz and Karson, 1997) according to Darcy's cubic law, whereas the permeability of soils relates to the grain-size distribution (Shepherd, 1989); consequently they all accomplish convective heat flow (Hardee, 1982).Variations of volcanic and geothermal activity have been frequently observed at sites such as Vulcano Island, Italy (Bukumirovic et al., 1997; Harris and Maciejewski, 2000), at Iwodake Volcano, Japan (Matsushima et al., 2003), at the Solfatara of Pozzuoli, Italy (Chiodini et al., 2007, 2011), at Colima, Mexico (Stevenson and Varley, 2008; Walter et al., 2013); but they were dubitably attributed to changes in the magmatic or hydrothermal source (Stevenson, 1993), to the permeability changes due to conduit sealing by deposition or tectonic activity (Harris and Maciejewski, 2000), or a combination thereof.

In this work we will build upon the testing the stratigraphic and volcanotectonic setting in controlling the permeability of degassing sites at Nisyros Island. We first explore if thermal mapping and soil analysis allow us to constrain the geological site conditions. On one hand, we make use of a portable infrared (IR) camera, which is efficient in imaging volcanic regions at metric to sub-metric resolutions, overcoming the low spatial resolution of satellites and the cost- and time-consuming thermometer-based measurements. On the other hand we collect and sieve soil samples to define soil types and related permeabilities. Finally we compare the spatial permeability contrasts with the spatial distribution of the thermal anomalies. Studies were made at the Stefanos crater on Nisyros (Fig. 1). This volcanic island has a long hystory of phreatic eruptions, the latest in 1871–1873 and 1887 (Marini et al., 1993), experiencing its last unrest in 1996–2001 (Papadopoulos et al., 1998; Chiodini et al., 2002; Sachpazi et al., 2002). The Stefanos crater is one of several phreatic craters on Nisyros, and is also the major contributor to the total heat budget of the island (Lagios et al., 2007; Ganas et al., 2010). Below we first introduce the study area, the infrared and soil analysis methods, followed by our interpretation of how the permeability might control the appearance of thermal anomalies.

2 Study area

2.1 Geological background

Nisyros is a volcanic island located in the eastern Aegean Sea (Fig. 1). The island is sub-circular in plain view with a diameter of ~ 7 km and morphologically appears like a truncated cone. The island represents the easternmost termination of the Hellenic volcanic arc related to the northward subduction of the Mediterranean plate underneath the European plate. The volcanic edifice developed through five stages (Marini et al., 1993; Tibaldi et al., 2008) that lead to the formation of a central caldera, ~ 4 km diameter, hosting some rhyodacitic domes and an alluvial plain, in the western and eastern part respectively. Superheated geothermal fluids have triggered hydrothermal explosions forming several phreatic craters, most recently in 1887 (Marini et al., 1993). The largest of these craters is the Stefanos crater, with a diameter of ∼ 300 m (Fig. 1), which is in the focus of our study.

2.2 Hydrothermal activity

The remarkable hydrothermal activity, i.e. hot springs and fumaroles, motivated site studies and the drilling of two deep wells for geothermal exploitation (Marini et al., 1993). These gave a direct view into the hydrogeological and hydrothermal system. Later, geochemical analysis (Chiodini, 1993; Lagios et al., 2007) helped to characterize the system, and the fumaroles on Nisyros were investigated in detail (Chiodini, 1993; Chiodini et al., 2002; Brombach et al., 2003; Teschner et al., 2007).

The hydrogeological system appears heterogeneously distributed both laterally and vertically (Marini et al., 1993; Ambrosio et al., 2010). On the eastern side of Lakki plain (W1 in Fig. 1b), there is a deep permeable zone in the diorite at 1400–1600 m depth that propagates shortly in the overlying carbonatic rocks. Another shallow permeable zone is located at 430–700 m depth within the tephra and lavas. No permeable zone is in the uppermost caldera filling deposits. Within the diorite on the western side of Lakki plain (W2 in Fig. 1b), there is one deep permeable zone, but at 1000–1300 m depth and propagating in the overlying tephra and lavas; the shallow permeable zone is instead at 30–360 m depth within the younger uppermost deposits (talus and alluvial) filling the caldera. The deep aquifer located at > 1000 m below sea level is heated (300–350 °C) and fed with fluids coming from the depths (Lagios et al., 2007). This lower aquifer provides vapor to the shallower aquifer, which has a temperature in the range of 150–260 °C (Chiodini et al., 2002; Lagios et al., 2007). Lagios et al. (2007) proposed that another shallow aquifer is fed by condensates.

At the surface, fumaroles occur mainly at the phreatic craters, such as, Stefanos, Phlegethon, Polybotes Micros (St, Ph, Pm in Fig. 1b), and at the eastern base of Lofos dome (LD in Fig. 1b). Temperature measurements at the phreatic craters have been conducted for decades, recording fumarole outlet temperatures of mostly 96–100 °C (Chiodini et al., 2002; Teschner et al., 2007). Smaller fumaroles occur along the flanks and on the top of the Lofos dome and at Kaminakia crater flank (LD, Kk in Fig. 1b). Some degassing vents occur also along the southern and western internal flank of the caldera following the NE–SW trends, which represents one of the main fault strikes recognized by Lagios et al. (2005).

An almost 100 yr period of quiescence ended with the 1996–2001 unrest episode. During this period, field observations report an increased fumarole activity in 1997 (Vougioukalakis and Fytikas, 2005). Other phenomena attributed to the unrest include the sudden opening of a tectonic-erosional fissure in the Lakki plain (Fig. 1) from November 2001 onwards (Galanopoulos and Kolettis, 2005; Vougioukalakis and Fytikas, 2005). Recent monitoring of the fumaroles at Nisyros since 2003 (Teschner et al., 2005, 2007) indicate that the outlet temperature is almost stable around 100 °C but fluctuates by few degrees according to extrinsic (meteorological) conditions. Satellite TIR data from 2000 to 2005 indicate that the Stefanos crater hosts a high temperature anomaly and contributes the most to the total heat flux budget of the caldera (Lagios et al., 2007; Ganas et al., 2010). In the same period, geophysical surveys reveal short term gravity changes (Gottsmann et al., 2005), occasionally associated with height changes, inferred to instabilities of the hydrothermal system (Gottsmann et al., 2007). However these variations do not appear in the temperature data of Teschner et al. (2007). More recent ground-based InSAR measurements (2010) could detect small-scale displacement signals, implying a general decrease of activity and suggesting that the hydrothermal system is close to rest conditions (Pantaleo, 2013).

Overall we observe that at caldera scale the lithologies determine the permeability contrasts, which are spatially distributed according to the stratigraphic conditions, and suggest that similar contrasts may generate at crater scale because small scale lithological heterogeneities. The Stefanos crater (Fig. 1) is a ∼ 30 m deep crater that has sub-vertical flanks and is slightly elliptical with the major axis – approximately 300 m – elongated in the NE–SW direction. Here we describe an IR and granulometry study at this crater to address the effect of outcropping deposits and structural features on the thermal field.

3 Method

3.1 Infrared (IR) survey

A forward-looking infrared camera (FLIR P620) was used to collect images in normal and panorama mode (Fig. 1). The camera operates at 7.5–13 µm bandwidth; the image size is 640 × 480 pixels and the resolution is 0.33 or 0.65 mrad (different lenses were used from different distances); the dimension of the pixel side is given by the resolution (mrad) times the distance of the target (*D*). The camera also hosts a digital optical sensor, allowing joint acquisitions of target regions. In total we recorded > 200 images to ensure ideal clear viewing conditions and the feasibility of image stitching, in order to investigate the thermal field at different scales (Figs. 2–4). On average 4–10 images were necessary to create mosaicked panoramas (Fig. 3) for both infrared and optical images, and ∼ 30 images to create the synoptic IR map of high spatial resolution (Fig. 4).

A dataset of images was collected on April 2010 in the day and night time. Images from long distance (*D*) were collected from the caldera rim close to Nikia (Fig. 1); here we used a telezoom to obtain a spatial resolution ∼ 0.7 m (Fig. 2). Images from shorter distances were recorded in panorama mode from two opposite vantage points along the crater rim. One subset was recorded from a position hundreds of meters southeast of the crater (Fig. 1b) showing the center of the crater and the west-facing Stefanos crater flank (Fig. 3a and b). The other subset viewed the crater from the northwestern side of the Stefanos crater rim (Fig. 1b) showing the bottom of the crater and its south-eastern flank (Fig. 3c and d). For these subsets, the pixel dimension ranged between 5 and 15 cm. Differences exist between the panoramas because the vantage points had different distances leading to a different field of view (FOV) and incidence angles.

A 360° panorama was recorded at the bottom of the crater (Fig. 1b), and these images were used to generate an IR mosaic of the entire crater (Fig. 4) and to detail small scale features on the crater floor (Appendix).

The IR images display temperatures in a color-coded scale, and these temperatures are considered relative. For each pixel, the temperature value represents the thermal energy distribution integrated over the pixel footprint (Dozier, 1981), accordingly:

$$\mathrm{Tobj} = \mathrm{Av} \cdot \mathrm{Tv} + (1 - \mathrm{Av}) \cdot \mathrm{Tb} \tag{1}$$

where (Tobj) is the pixel temperature, Av and (1 – Av) are the vent area and the vent-free area within the unitary pixel, respectively; Tv and Tb are the temperature (°C) of the vent and of the background, vent-free area, respectively. Otherwise Tobj depends on parameters like the target-to-sensor distance (D), the emissivity of the target (ε), and the transmittance of the atmosphere (τ) as a function of atmospheric temperature (Tatm) and relative humidity (RH). Finally the accuracy of the measurements depends on the orientation of the FOV, which should be as parallel as possible to the target (Ball and Pinkerton, 2006).

For each dataset acquired in panorama mode, the images were sampled in fast sequence steering the IR camera, allowing a small overlap between consecutive pictures. Because the distance was almost constant for each of the shooting positions and the time required for each acquisition is short, a few seconds, the parameters D, Tatm and RH were assumed constants. Values of Tatm and RH are assumed to be suitable to site conditions in the range of 10–20 °C and 50 %, respectively. Also ε is assumed to be constant and equal to 0.93 according to literature (Lagios et al., 2007). All these assumptions were valid also for the images constituting the other datasets and collected as independent snapshots. We did not consider a pixel-by-pixel correction approach. Also, geometric complexities, arising from the different viewing field and topography, were not corrected for.

We processed the raw images by FLIR ThermaCAM software. The results are displayed (Figs. 2–4) with temperature scales saturated and clipped at the 10–60 °C interval for the night panorama, and at 15–60 °C, 15–90 °C for day panoramas, respectively, to enhance the thermal patterns. The stitching of infrared and digital images is finally executed using a combined perspective-cylindrical merging tool as embedded in common image softwares (Photoshop). The images taken from within the crater floor were also used to generate a crater-wide mosaic that is subsequently georeferenced in map view (Fig. 4) with GIS software (ArcGIS 9.3 by ESRI). This necessitates the application of a matching procedure of ground control points (GCPs), i.e. manually selected features, recognized in both the satellite image (WorldView02, visible bands) and the IR mosaic.

A second field survey in January of 2013 allowed for the collection and verification of the IR images collected in 2010. This follows a similar procedure except that the vantage positions are now at the northern and southern border of the crater. Besides the crater floor could not be comprehensively imaged because it was partially flooded by recent rainfall.

3.2 Soil analysis

The soil samples (12) were collected (Fig. 5) during our campaign in January 2013. Sampling locations were chosen at the crater floor mainly along an E–W profile (Fig. 6) crossing fumarole-bearing and fumarole-free areas. Two samples were collected along the eastern flank and two more samples in the southern and northern sector, corresponding with sites of anomalous and normal temperature, respectively (Fig. 6). The sampling sites were selected according to the need of (i) representing the different thermal conditions and expressions (fumarole, diffusely heated ground, mud pools, boiling runoff) highlighted by the 2010 infrared survey; (ii) having a sampling dense enough for spatial comparison to thermal data, and (iii) limiting the total weight. Indeed the E–W profile allowed to intersect the thermal anomalies at the crater border, the center, and the interposed cool areas. A N–S profile instead would have neglected the large thermal anomalies observed at the western and eastern flank base. Moreover the sampling would have suffered for larger discontinuity because of the flooded area that was elongated in N–S direction. Finally due to lack of instrumentation, we could not execute the laboratory analysis on-site and the weight of samples was limited for transport reasons. However the representativeness of the bulk grain size distribution was ensured by collecting masses (g) of at least 100 times the maximum particle size (mm) for each sample.

Each sample was collected at a depth up to 20 cm from the surface. We ensured that the sample corresponded to a single soil type, e.g. silty sand or clay, based on a visual description of pits dug. Thereafter we increased the depth of the pit to 50 cm in an attempt to check for a possible vertical gradient in the temperature. From each location, we took about 1–2 kg of soil sample for further laboratory analysis. Initially the sample was oven-dried to remove the humidity, then weighted. The drying was executed at $\sim 70\,^{\circ}\mathrm{C}$ to avoid the melting of sulfur crystals. The samples were then sieved (ASTM-D6913-04, 2009) to discern the relative percentage of granular fractions, particles with diameter (d) larger than 0.064 mm, and cohesive fraction, particles with d smaller than 0.064 mm. The cohesive component is washed away by running water filtered by sieves, while the granular material is kept on them. Finally the soil trapped by each sieve is dried and weighted again.

We used 4 sieves with mesh openings of 2.0, 0.5, 0.25 and 0.064 mm which allowed to separate gravel and coarse sand fraction ($d > 2.0$), medium sand fraction ($2.0 < d < 0.5$), fine sand fraction ($0.5 < d < 0.064$), silt and clay fraction ($d < 0.064$). The maximum d for each sample was noted visually, few clasts exceeded 10 mm. We did not perform the settling analysis to compute the relative percentage of silt and clay.

Following the geotechnical practice, the results are presented as distribution curves in a semi-logarithmic plot (Fig. 6); the vertical axis indicates the cumulate percentage (by weight) of soil passing through the sieve whose mesh size is labeled on the horizontal axis. In this plot, we adopt $d = 10$ mm as maximum value and assume that all the material is smaller, so the grain-size curve results interpolated from $d = 2$ mm to $d = 10$ mm (dashed curves in Fig. 6).

4 Results

The findings of our survey are presented starting with the IR observations performed from large distance to observe the general temperature field, and then concentrating on shorter distances and close-up. Finally we present the grain-size results and their integration with the IR data.

4.1 Far field view of general thermal architecture

The IR images collected from the caldera rim, about 1000–1200 m far from the Stefanos crater (Fig. 1), have a coarse resolution with pixel side of about 0.65–0.78 m. They show the western flank of the crater and part of the bottom, the remaining parts are not imaged because of the topography-related shadowing effect (Fig. 2a and b). The upper rim of the crater does not express any thermal anomaly whilst the bottom rim of the crater does; the temperature field is shown by a ring not perfectly concentric surrounding the crater floor (Fig. 2b). The temperature distribution is smoothed and homogenized (Fig. 2c) because of the coarse resolution, therefore single or grouped vents cannot be recognized. On the western and southern sides, more elevated temperatures and wider thermal fields can be observed. At the southern side the relative temperature (T) is in the range 22–30 °C and rises to 30–40 °C westward (r in Fig. 2c) before decreasing to 24–30 °C northward. The background cool temperature inside the crater is ≤ 18 °C. Further clustered anomalies are observed toward the center of the crater; these display a relative T of 20–25 °C and mark the transition between the southern part, warmer, and the northern, colder.

4.2 Close field view of small scale structures

The mosaics (Fig. 3) produced with images collected close to the Stefanos crater have a high resolution of about 5 and 15 cm of pixel side. These mosaics show that the thermal anomalies are distributed in a roughly circular-shaped pattern at the margin of the crater floor (Fig. 3b and d). The anomalies are wider along the west, through the south, to the east side and narrower at the opposite side. Hotter spots corresponding to clustered vents are now distinguished as sparsely distributed within the geothermal field showing relative $T \geq 60\,^{\circ}\mathrm{C}$. The western side hosts a mound of material (r in Fig. 3a and b), 2–3 m high, ≤ 10 m wide and ~ 50 m long, covered by a hard crust dotted by centimeter-size vents; around the mound the crater floor is diffusively heated at relative $T \sim 40\,^{\circ}\mathrm{C}$. The southern side (Fig. 3c and d) has a rough surface with extensively developed hard crust covered by pebbles/boulders fallen from the adjacent flank; there are few vents and the heat is released diffusely, so relative T is $\sim 30\,^{\circ}\mathrm{C}$. The eastern side is flat except for a mound (n in Fig. 3c and d), 0.5–1 m high, 2–3 m wide and ~ 30 m long, hosting vents; at the base of this flank there are also superficial boiling runoff and small boiling ponds (up to tens of cm size). The relative T of the thermal anomaly at this side is $\geq 40\,^{\circ}\mathrm{C}$. Toward the center of the crater embedded in the cooler terrain, we identify thermal anomalies – relative $T \sim 30\,^{\circ}\mathrm{C}$ – corresponding to sub-metric to metric wide boiling ponds (p in Fig. 3d) fed by meteoric water and superficial runoff. Another localized anomaly is isolated along the northeastern flank on the slope, (g in Fig. 3b and d); its relative temperature appears to be 25–30 °C or higher, depending on the viewing geometry. Temperatures are generally lower than inferred from pointwise measurements because the vent usually occupies a small part of the pixel (cfr 3.1) and contributes proportionally to the pixel thermal budget. Moreover, T values were saturated and clipped in the range of 10–15 to 60 °C to achieve an optimum visualization of the thermal and morphological features. Vice-versa, the IR close-up of fumarole clearly displays T values of $\sim 100\,^{\circ}\mathrm{C}$ (Appendix).

Both the optical panoramas (Fig. 3a and c) show the above-mentioned morphologies (mounds r, n) as well as the sites with high sulfur content (yellowish) at the crater floor and along the flanks, which are not detectable in the infrared panoramas.

4.3 Mosaic of large to small scale structure

All the thermal features are finally displayed in the georeferenced IR mosaic (Fig. 4) giving a synoptic view of the crater. A total of > 30 images have been fused and ≥ 5 GCPs have been selected to reference each image. The IR map shows most of the crater except a small patch in the cold region which was not covered by any image. The geothermal field, expressed by the ring-shaped thermally active zone, is fully visible running along the border of the crater floor. The ring is not perfectly symmetric, but appears wider in the W–NW (r in Fig. 4), S and SE (n in Fig. 4). In the N–NW and SE, two opposing flanks are expressed by highest temperatures recorded, marking elevated thermal fields trending SW–NE. We note that the same SW–NE trend is already identified by the long axis of the ellipticity of the crater and by one of the main structural trends seen elsewhere on the island. The mosaic shows also the boiling ponds (p in Fig. 4), standing out from the cold zone close to the crater center, and the thermal anomaly along the NE flank (g in Fig. 4). The spatial analysis reveals that the extent of the thermally anomalous area along the western flank is $\sim 2400\,\mathrm{m}^2$, whereas on the opposite flank is $\sim 2700\,\mathrm{m}^2$; meanwhile, the anomalies at the southern and northern sites cover $\sim 500\,\mathrm{m}^2$ each, whereas the anomaly at the center is $\sim 70\,\mathrm{m}^2$. The overall heated ($> 30\,^\circ\mathrm{C}$) surface is $\sim 6200\,\mathrm{m}^2$ and corresponds to 17 % of the $\sim 35\,300\,\mathrm{m}^2$ wide crater floor, or 10 % of the $\sim 59\,000\,\mathrm{m}^2$ crater and flank surface (semi-axis are of 125 and 90 m whilst the height of the flank is ~ 30 m). We selected 30 °C as the threshold because it effectively separates the geothermal effect from the insolation and characterizes the thermal anomalies at this spatial resolution.

We also show three cross sections (Fig. 4) to highlight the spatial relation between the thermal anomalies and the topography. Two cross sections (a–a', b–b') are oriented NW–SE, while one (c–c') is oriented SW–NE. All the sections show that temperatures augment moving down the flank, the increase is gradual or sharp according to the insolation artifacts. That is more evident along b–b', where T fluctuations along the northwestern flank indicate heated and shadowed layers. The highest temperatures are reached at the breaks in slope, but the extents are different, as a–a' crosses the wide anomalies (r, n), whereas b–b' and c–c' do not. The temperatures have the tendency to diminish toward the crater center and to flatten at 10 °C (clipped value imposed by our elaboration) in the cool areas; the only exception are the T peaks in correspondence of the boiling ponds (p). Profile c–c' also shows the thermal anomaly (g) that occurs along the flank and reaches values comparable to the anomalies at the flank toes.

4.4 Soil analysis

We present the results from the soil analysis in the form of a semi-logarithmic grain-size curve (Fig. 6) and in an ArcGIS framework on the IR map to provide a combined view of temperature – grain-size distributions (Fig. 6). The grain-size plot (Fig. 6) shows two main groups: the cohesive type, which has $\geq 60\,\%$ of cohesive fraction, and the granular type, which has $\leq 40\,\%$ of cohesive fraction. Both soil types are generally well graded when considering the sand fraction, with the exception of S01, S12, which have a dominant medium and fine sand fraction. In a first-order approximation, we describe the granular type as medium-to-fine sand and the cohesive type as a silt-clay. The granular type has higher permeability (k) than the cohesive type because it allows higher porosity. We refer to tabulated values (Bowles, 1988) indicating $k \sim 10^{-5}$–$10^{-7}\,\mathrm{m\,s^{-1}}$ for sands (variation depends on the amount of cohesive fraction) and $k \sim 10^{-11}\,\mathrm{m\,s^{-1}}$ for silt and clay.

Spatially we observe that the sample S01 (Fig. 5) collected at the base of the western mound has 93 % granular content with cohesive material being almost absent. The sample S12 collected at the southern border and below the hard crust has 85 % granular content, again with very low cohesive fraction. At the eastern flank, the samples S07, S08 (Fig. 5), S09 and S10 are granular with percentages ranging between 64 and 80. The samples S04 and S05 are collected as close as possible to the ponds, just a few meters, but out of the area temporarily flooded by the rain. They have granular content below 40 % and significant cohesive content of about 60–70 %. A similar value is found in a deeper sample (S04 at 50 cm) collected because the IR data showed a temperature increase, ~ 35 °C, thus suggesting a reduction of the vertical efficiency in heat transfer. The samples S02 and S03 (Fig. 5) collected between the western flank and the mud pools have cohesive percentages ranging between 70 and 80. The sample S06 (Fig. 5) collected between the eastern flank and the mud pools is ~ 90 % granular. The soil sample S11, at the north of the mud pools where there is no thermal anomaly, has ~ 68 % of cohesive particles.

4.5 Comparison of IR and soil analysis

Overall the granular soils are found with thermal anomalies and vice-versa (Fig. 6). We notice that S06 diverges from the general behavior by having a high granular fraction but being located in a cool area. In this case, we might be observing the cooling effect of the rain rather than an error in the sieving operation; indeed S06 was located close to the flooded area. We also note an apparent correlation between changes in the granular % with the spatial thermal gradient. Looking at the granular content along the E–W profile (S01–S08), we note that it decreases drastically (~ 65 %) from S01 to S02, which are ~ 40 m apart, then it gradually decreases from S02 to S03 and increases, from S03 to S06, at rates of 10 % each ~ 20 m. Higher rates (20–30 % each 20 m) occur between S06-S07-S08. These observations are in agreement and reflect the patterns of the displayed thermal gradients. (Fig. 4 profile *a*–*a*′). Indeed we imaged strong horizontal thermal gradients, 30–40 °C, from S01 to S02 and from S06 to S07, whilst from S02 to S06, it fluctuates in the range of ~ 15 °C. The granular content along the N–S profile (S08–S10) appears more stable as indicated by the horizontal thermal gradient too.

5 Discussion

This work is for the first time elaborating in detail the relationship between the thermal field and the soil permeability of the biggest explosion crater on Nisyros island. The

Stefanos crater is known for its widespread geothermal field, the fluid emissions and the short term episodes of uplift and gravity changes. We analyzed the thermal field by means of a multi-scale infrared study, mosaicking over tens of images retrieving spatial resolutions (pixel size) of 0.05 to 0.8 m, approximately. Results show a complex arcuate high-temperature field surrounding the center of the crater floor, common at many volcanoes elsewhere, which at Stefanos crater is stronger expressed at the NW and SE sides. Here the temperature is not only higher but the thermal field is also wider. To test this temperature distribution in more detail, we collected soil samples and identified the granulometry. We find a first order correlation between the grain-size distribution of the soil, which we consider a proxy for soil permeability, and the temperature distribution.

Understanding the dynamic of the degassing close to the surface at Nisyros is of relevance, as the volcano is currently ranked in the "Very High Threat" class (Kinvig et al., 2010), considering the vulnerability of the population (∼ 1000) and of the tourists (∼ 60 000). Stefanos crater was chosen to perform the IR study because of the increase in fumarole activity and the outflow of melted sulfur and hot mud during the last unrest (Papadopoulos et al., 1998; Chiodini et al., 2002; Sachpazi et al., 2002; Vougioukalakis and Fytikas, 2005; Lagios et al., 2007), as well as its strong thermal signature in comparison to other phreatic craters (Lagios et al., 2007; Ganas et al., 2010). Moreover our results may have implications relevant for other sites. Indeed Stefanos crater is a rather typical phreatic crater with a morphometry similar to those found on other volcanoes. Stefanos crater also displays a ring-shaped thermal pattern of fumaroles similarly observed at other volcanic craters, such as at Vulcano (Bukumirovic et al., 1997), Satsuma-Iwojima (Shinohara et al., 2002), Colima (Varley and Taran, 2003), Kudrayavy (Yudovskaya et al., 2008).

In the following we first discuss the limitations which might affect our data and their contribution to our interpretation. Later, based on the results of our IR survey, the field observations and the laboratory tests, we elaborate how the thermal field at the Ste-

Title Page
Abstract Introduction
Conclusions References
Tables Figures
◀| |▶
◀ ▶
Back Close
Full Screen / Esc
Printer-friendly Version
Interactive Discussion

fanos crater is controlled by stratigraphic conditions, the latter driven by depositional processes which superimpose the structural control.

5.1 Limitations

Limitations may arise from the infrared technique, the environmental conditions, the image processing and mosaicking, or a combination thereof. Moreover, soil sampling and laboratory analysis may affect the conclusions drawn, as detailed below.

5.1.1 IR imaging

The main limitations affecting IR imaging relate to the changes of emissivity and transmittance, which depends on geometric conditions, i.e. distance and viewing angle, and on physical condition of the target and of the atmosphere. Here we detail the limitations encountered at Nisyros and their influence on the results. A detailed description of general limitations is provided by Spampinato et al. (2011).

The IR mosaics we present are computed using a constant camera position. However, D changes within a single image and across each set of images from foreground to background, and Tobj is expected to vary consequently. In our dataset we found that, doubling D, the Tobj varies in the range of 1–3 % according to the occurrence of Tobj close to or higher than Tatm. For the processing, we use the mean distances in the field of view. Therefore at shorter distances, the temperature is expected to be overestimated, and vice-versa. We note that these differences are small and therefore negligible for the purpose of this study. Moreover D influences the geometric resolution: while increasing D causes the widening of the pixel size and, consequently, the likelihood of including larger cold surface, it is also possible to include more vents but less likely. That leads to a lower sensitivity in the detection of relative temperature contrasts. Further errors arise from assuming a single emissivity value because it changes with the material and the viewing angle (Ball and Pinkerton, 2006). We use $\varepsilon = 0.93$ for the average site conditions following previous works (Lagios et al., 2007). Laboratory tests showed that emissivity is expected to decrease as the viewing geometry deviates from the perpendicular to the surface (Ball and Pinkerton, 2006). Such a phenomenon should affect the crater floor due to the oblique viewing, but it should not affect the flanks, as the viewing geometry is almost perpendicular. Nevertheless we do not observe any temperature gradient which may relate to the viewing angle. Another issue related to the site conditions is the presence of steam in the line of sight which dampens the propagation of the thermal signal (Sawyer and Burton, 2006). As shown by the digital panoramas (Figs. 2a, 3a and c) we managed to collect our IR data during low-to-absent (visible) steam output, although we cannot rule out its contribution.

Considering the atmospheric conditions, we corrected the transmittance using values of temperature and relative humidity suitable for the site conditions (cfr, 3.1). This does not affect our results because the purpose of this work is to investigate the spatial distribution of thermal anomalies. Indeed we tested that changes in Tatm of ±10 °C cause variations of Tobj ranging between 3 and 1 °C for cool ground and < 1 °C for heated ground.

Finally, in terms of data processing, the georeferencing appears accurate along the flank because there are matching features (layering) between hand-held IR and satellite OP image, as well as only a small amount of geometric distortion. We did not further analyze the accuracy of georefencing; at the crater floor this accuracy may be lower because of the lack in recognizable features. Moreover, the IR images taken from the crater floor may suffer from large geometric distortion due to the viewing geometry. Our data are actually collected from a short distance (a few hundred meters) with a lens providing a field of view of $24^\circ \times 18^\circ$, which is somewhat narrow and prevents large distortions.

5.1.2 Soil analysis

Soil samples were collected within the top 50 cm only. Sampling at a different depth might provide different information. However we are confident that the correlation of grain-size with the IR data is beyond coincidence.

Grain-size distribution of volcanic deposits is generally investigated to understand eruptive processes and energy (Brazier et al., 1983; Andronico et al., 2013) or to address the permeability of volcanic deposits (Antoine et al., 2009; Peltier et al., 2012), usually by means of mechanical sieving. A major limitation during our sieving operation was in the artificial modification of the grain-size distribution. Indeed, in our samples, native sulfur crystals and chemically weathered volcanic clasts (Fig. 6) were fragile and could break into smaller granular particles. Converesely, the cohesive material appears as aggregates simulating granular clasts. We attempted to minimize these issues with a careful washing to avoid strong particle collision and by using a brush to disperse the cohesive aggregates. The substantial difference of sand contents between the granular and cohesive type (Fig. 5) suggests that our sieving procedure prevented the convergence to a single sand class. Another source of error affecting the fraction distribution derives from having volcanic silicate particles with a density of 2.4–2.6 $\mathrm{g\,cm^{-3}}$ mixed with native sulfur crystal of 1.9 $\mathrm{g\,cm^{-3}}$ density. The density contrast could cause a 7 % difference in weight on equal volumes of silicate and sulfur, but as the quantity of silicate in our samples is much larger, the bias becomes negligible.

A systematic bias in the grain-size description of the soil would cause a different or even misleading estimation of permeability values and consequently affect the interpretation of the thermal field. The number and type of sieves used allow us to determine the type of soil collected but do not allow a rigorous classification according to an established standard, e.g. unified soil classification system (ASTM-D2487-83, 1985). Otherwise we might have overestimated the amount of gravel and coarse sand by having the largest sieve mesh at 2.0 mm and by fixing the maximum $d < 10$ mm based on visual description. We evaluate this effect to be ∼ 10 % for the cohesive type and up to ∼ 20 % for the granular type (∼ 40 % for S01). This error affects only the relative percentage of granular fractions, not the relative percentage of granular vs. cohesive, though we disregarded the occurrence of gravel to estimate the soil permeability. Under the aforementioned assumptions and supported by the extensive engineering literature relating soil grain-size to soil permeability (Shepherd, 1989; Odong, 2007), we consider that using tabulated permeability values is correct for qualitative assessment. The permeability can also be measured by laboratory or in situ tests, but both the procedures are technically demanding and too ambitious for our purpose (Lambe and Whitman, 2008). Note the values refer to water permeability, whereas air permeability, which is generally higher (Springer et al., 1998), should be considered. This approximation is nevertheless representative of the different behavior of the soil types identified at Stefanos.

5.2 Conceptual model

Stefanos crater has a phreatic genesis and is elongated NE–SW, coherent with a major fault trend observed elsewhere on the island. Marini (1993) suggested that a fault may have started the cratering by (i) connecting two aquifers and causing the flashing of the fluids, or (ii) weakening/opening the sealing of a deep, over-pressured, hot aquifer that flashed. One may assume that hot fluids continue to migrate upward through the fault into the crater (Fig. 7). In this scenario, we would expect to observe a linear thermal anomaly congruent with the trace of the fault trend. Our data show a near circular thermal anomaly mainly at the border of the crater, more pronounced at those sectors parallel to the presumed fault direction.

Our soil analysis suggests that (i) cohesive and impervious material seals the center of the crater by inhibiting the convective fluid ascent which is then diverted and forced laterally toward the crater border. (ii) There, granular and permeable materials effectively transfer the heat along the crater border. Indeed, we found a permeability contrast of 4–6 orders of magnitude. Consequently, the heat release appears to be controlled by the soil texture distribution related to depositional processes (Fig. 7). We infer that granular permeable material of the crater talus is widely deposited at depth, while upward its extension is limited to the crater border (Fig. 7). This material corresponds to the remobilized original talus of the caldera escarpment and remobilized deposits of the Kaminakia and Stefanos explosions. Afterwards, mixed granular and cohesive sediments drained by the superficial runoff into the crater from the surrounding relief and gradually filled the crater (Fig. 7). We observe that the soil particles range from pebbles to silt/clay and that there is a selective deposition based on the energy of the runoff; the particles travel either short or long distances from the crater border according to their dimension.

The IR observations indicate that the western, southern and eastern borders have a wider extension of the thermal anomaly, which might relate to a wider deposition of granular material. We conjecture that at those sites the sediment input is larger and has higher energy. Indeed we note that the topographic gradient outside the crater is steeper at the western, southern and eastern borders (Fig. 1b).

In addition, the thermal anomalies at the eastern and western flank parallel the suspected NE–SW trending fault (Fig. 7), binding the crater (Caliro et al., 2004). Indeed, this may also locally increase the permeability without requiring an increase of sediment volumes. Finally it is also possible a combination of sediment input and faults (Fig. 7). The depositional processes, however, cannot explain the mud pools at the center of the crater, and particularly the diffuse heating along the northeastern flank (p and g Fig. 3–5). We speculate that both the features can be addressed by a complex volcanotectonic control locally overprinting the soil texture control: fractures may intercept and facilitate fluid migration through an impermeable layer (Fig. 7).

5.3 Comparison with other results

5.3.1 Thermal data

The comparison of our ground-based survey with previous satellite-based observations (Lagios et al., 2007) only has a qualitative value because the geometric resolution differs by two orders of magnitude. Moreover, the viewing geometry of the camera is favorable to view the crater flank, whereas satellites have a better view of the crater floor. Nevertheless, both datasets reveal that the southern sector of the crater shows a more pronounced thermal flux than the northern sector. A single previous ground-based IR survey was performed at Nisyros in 2002, immediately after an episode of unrest, with the aim to validate satellite IR data (Lagios et al., 2007). Images were collected from the caldera rim at Nikia (Fig. 1) and showed all the Stefanos crater except the eastern flank and surrounding floor. The spatial resolution of the previous survey is one order of magnitude lower than the resolution of our images. Considering this difference, the amplitude of the anomalies still appears in the same range of values, and the spatial pattern has not changed dramatically. Only a small anomaly within the current cold region and some others in proximity to the upper crater rim have disappeared since then. That might indicate a small decrease of activity following the unrest and simultaneously exclude a significant decline in heat flux since 2002. The general pattern of temperature distribution remains mostly constant. The anomaly at the crater floor occurred where we expect the deposition of cohesive sediment, thus confirming our hypothesis on the depositional sealing. The comparison of our 2010 and 2013 survey, where possible, also does not show significant change in the extent of the thermal field; confirming the stability of the degassing system and suggesting that depositional sealing acts at a low rate.

5.3.2 Lithological control

At Nisyros we describe the thermal field of Stefanos crater and the concurrence with the soil texture causing permeability contrasts on the order of 10^4–$10^6\,\mathrm{m\,s^{-1}}$. The role of soil texture in controlling the thermal permeability was also suggested elsewhere, e.g. at White Island, New Zealand (Mongillo and Wood, 1995), between lacustrine sediment and fractured lavas. At Yenkahe, Vanuatu (Peltier et al., 2012), differences in soil permeability and thermal expression were observed involving scoria layer and ash layer. Whereas at these two sites the permeability contrasts are inherited mostly from primary eruptive products and processes, at Stefanos, it is inherited from sedimentary depositional processes. A temporal development of sediment accumulation and, accordingly, a temperature field change at volcanic craters is open for speculation. In the first stage, we suspect the occurrence of crater inward sliding of peripheral blocks as observed at Anatahan, Northern Mariana Island (Nakada et al., 2005) and at Miyakejima, Japan (Geshi et al., 2012). In a later stage, the crater collects sediments through ephemeral fluvial-to-deltaic depositional processes, which activate with seasonal rainfalls. Our work hence suggests that permeability contrasts generated by depositional processes may be relevant for the evolution of the fumarole field elsewhere, possibly even being independent from the crater's genesis. Specifically, the progressive reduction of permeability might be a factor of risk, because, while reducing the appearance of the heat signature, it also contributes to the seal. The sealing of hydrothermal sources may lead to overpressure the hydrothermal system, facilitating phreatic explosions.

5.3.3 Structural control

While the role of soil texture has been generally underestimated, many previous studies at White Island, New Zealand (Mongillo and Wood, 1995), at Etna, Vulcano, Stromboli, Italy (Finizola et al., 2003; Calvari and Pinkerton, 2004; Aubert et al., 2008; Harris et al., 2012), at Kudryavy, Kurili Island (Yudovskaya et al., 2008), and Yenkahe, Vanuatu (Peltier et al., 2012) identified and attributed the thermal anomalies to structures facilitating the migration and escape of fluids. The structures are usually associated with crater rims or fault planes, which either have a geomorphologic expression at the surface or may be buried.

5.3.4 Stress control

Previous authors have also studied the influence of the gravitational stress field on fluid up rise (Schöpa et al., 2011). We address this topic at Nisyros only qualitatively because the topography of Stefanos crater is minor. The crater is excavated ~ 30 m below the mean caldera topography, and little is known about the mechanical parameters of the sediments. A suitable analogue for this morphology is represented by open pit mines, so we can adopt results from these studies (Stacey et al., 2003) to our case study. Firstly, the stress field generated by facing flanks does not interplay when the flanks are distant ~ 0.8 times their height. At Nisyros, that condition is verified both at the caldera scale and at the scale of the Stefanos crater. Secondly, close to the surface, the trajectories of the maximum principal stress ($\sigma1$) follow the topography, being subvertical at the crater walls and horizontal at the crater floor. At the same time, the stress field inside the crater appears compressive and counteracts the degassing, similarly to what observed at Vulcano (Schöpa et al., 2011). However, a substantial difference exists between the two sites; at the crater floor of Stefanos, the thermal anomalies are clearly expressed, in contrast with the stress regime, whereas at Vulcano, there are no thermal anomalies seen in the crater floor, in agreement with the stress regime.

5.4 Implications for future studies

We think that including more case studies might improve the comprehension of the factors influencing the fluid paths according to genetic and morphological classes. We suggest that, while a single survey can be useful to understand the setting of the degassing system, repeated surveys can witness the evolution of the fumarole field. The thermal field of some volcanoes, e.g. Vulcano Island, Iwodake, and Colima (Harris and Maciejewski, 2000; Matsushima et al., 2003; Stevenson and Varley, 2008) have experienced temporal and spatial changes. Such changes can also occur elsewhere, and our results suggest that the observation and monitoring of lithologies, structures, and stresses can improve the understanding of those changes. As a rule of thumb, the appearance of the thermal field should be reduced by the deposition of new sediments acting as insulating layer, vice versa a removal of material should augment the appearance. The deposition or removal of large volumes may be associated with sliding or eruptive processes, which have the potential to modify the structural setting and the stress field.

From a technical perspective, the thermal monitoring can benefit from the use of IR mapping and GIS processing because of their wide coverage and the ability to generate historical databases that easily integrate different information. This would undoubtedly benefit the hazard assessment by improving the interpretation of infrared data in terms of increased activity or increased permeability.

6 Conclusion

We used IR measurements to map the spatial arrangement of the thermal field at the phreatic crater of Stefanos on Nisyros island (Greece). The combination of IR images and soil grain-size analysis suggests that the temperature field is controlled by the depositional processes of sediments and, possibly, by faults. Indeed, the warmer areas occur at the bottom rim of the crater within permeable soil, while the colder ones occur within the cohesive sediments at the center. Localized thermal anomalies, boiling mud pits opening at the crater center, are associated with volcanotectonic features (fractures), which drive erosional processes along one of the island-wide fault trends. With earlier studies in mind, three main factors control fumaroles: lithology (our study), geological structures, and stress field (Schöpa et al., 2011). We suggest that the parameters controlling the fumarole sites might be applicable elsewhere, though their hierarchy and efficiency may vary according to the genesis of the volcanic morphology and the surrounding geological setting.

Appendix A

Using the images collected within the crater, we can further explore particular features which are not revealed from larger distances. Indeed the resolution ranges from a few millimeters to centimeter when standing above the targets. The IR measurements taken directly above the fumaroles show that the vent relative T decreases rapidly from $\sim 100\,^{\circ}$C to 30–40 $^{\circ}$C sideways (Fig. 8). Such vent temperature is in agreement with the temperature measured inside the vent by the K-type thermocouple during our survey, and confirms findings by previous authors (Chiodini et al., 2002; Teschner et al., 2007). Similarly, the close-up of the mud pits show the temperature decreasing rapidly from $\sim 60\,^{\circ}$C at the deep-seated boiling surface to almost to 20 $^{\circ}$C at the surface. The ground surrounding the ponds is cold and a network of cracks separate desiccation polygons (Fig. 8), usually 10 to 20 cm side, whose surfaces have sulfur films developing from the crack inside the polygon. The cracks are warmer than the plate and we also observed the soil temperature increasing ~ 5–10 °C few centimeters below the crust. Such a pattern resemble on a small scale the one observed at the crater scale.

Acknowledgements. The authors want to thank A. Klatten for helping in the field activities, G. Frijia and C. Fischer for the use of laboratory facilities at the University of Potsdam.

References

Ambrosio, M., Doveri, M., Fagioli, M. T., Marini, L., Principe, C., and Raco, B.: Water–rock interaction in the magmatic-hydrothermal system of Nisyros Island (Greece): J. Volcanol. Geoth. Res., 192, 57–68, 2010.

Andronico, D., Taddeucci, J., Cristaldi, A., Miraglia, L., Scarlato, P., and Gaeta, M.: The 15 March 2007 paroxysm of Stromboli: video-image analysis, and textural and compositional features of the erupted deposit, B. Volcanol., 75, 1–19, 2013.

Antoine, R., Baratoux, D., Rabinowicz, M., Fontaine, F., Bachèlery, P., Staudacher, T., Saracco, G., and Finizola, A.: Thermal infrared image analysis of a quiescent cone on Piton de la Fournaise volcano: evidence of convective air flow within an unconsolidated soil, J. Volcanol. Geoth. Res., 183, 228–244, 2009.

ASTM-D2487-83: Standard practice for classification of soils for engineering purposes (Unified Soil Classification System), American Society for Testing and Materials, D. 2487-83, 1985.

ASTM-D6913-04: Standard Test Methods for Particle-Size Distribution (Gradation) of Soils Using Sieve Analysis, American Society for Testing and Materials, D 6913-04, 2009.

Aubert, M., Diliberto, S., Finizola, A., and Chébli, Y.: Double origin of hydrothermal convective flux variations in the Fossa of Vulcano (Italy), B. Volcanol., 70, 743–751, 2008.

Ball, M. and Pinkerton, H.: Factors affecting the accuracy of thermal imaging cameras in volcanology, J. Geophys. Res.-Sol. Ea., 111, doi:10.1069/2005JB003829, 2006.

Bowles, J. E.: Foundation Analysis and Design, McGraw-Hill Book, England, 1988.

Brazier, S., Sparks, R. S. J., Carey, S. N., Sigurdsson, H., and Westgate, J. A.: Bimodal grain size distribution and secondary thickening in air-fall ash layer, Nature, 301, 115–119, 1983.

Brombach, T., Caliro, S., Chiodini, G., Fiebig, J., Hunziker, J. C., and Raco, B.: Geochemical evidence for mixing of magmatic fluids with seawater, Nisyros hydrothermal system, Greece, B. Volcanol., 65, 505–516, 2003.

Bukumirovic, T., Italiano, F., and Nuccio, P.: The evolution of a dynamic geological system: the support of a GIS for geochemical measurements at the fumarole field of Vulcano, Italy, J. Volcanol. Geoth. Res., 79, 253–263, 1997.

Caliro, S., Chiodini, G., Galluzzo, D., Granieri, D., La Rocca, M., Saccorotti, G., and Ventura, G.: Recent activity of Nisyros volcano (Greece) inferred from structural, geochemical and seismological data, B. Volcanol., 67, 358–369, 2004.

Calvari, S. and Pinkerton, H.: Birth, growth and morphologic evolution of the "Laghetto" cinder cone during the 2001 Etna eruption, J. Volcanol. Geoth. Res., 132, 225–239, 2004.

Chiodini, G., Cioni, R., Leonis, C., Marini, L., and Raco, B.: Fluid geochemistry of Nisyros island, Dodecanese, Greece, J. Volcanol. Geoth. Res., 56, 95–112, 1993.

Chiodini, G., Brombach, T., Caliro, S., Cardellini, C., Marini, L., and Dietrich, V.: Geochemical indicators of possible ongoing volcanic unrest at Nisyros Island (Greece), Geophys. Res. Lett., 29, 1759, doi:10.1029/2001GL014355, 2002.

Chiodini, G., Vilardo, G., Augusti, V., Granieri, D., Caliro, S., Minopoli, C., and Terranova, C.: Thermal monitoring of hydrothermal activity by permanent infrared automatic stations: results obtained at Solfatara di Pozzuoli, Campi Flegrei (Italy): J. Geophys. Res.-Sol. Ea., 112, B12206, doi:10.1029/2007JB005140, 2007.

Chiodini, G., Avino, R., Caliro, S., and Minopoli, C.: Temperature and pressure gas geoindicators at the Solfatara fumaroles (Campi Flegrei), Ann. Geophys.-Italy, 54, 151–160, 2011.

Curewitz, D. and Karson, J. A.: Structural settings of hydrothermal outflow: Fracture permeability maintained by fault propagation and interaction, J. Volcanol. Geoth. Res., 79, 149–168, 1997.

Dozier, J.: A method for satellite identification of surface temperature fields of subpixel resolution, Remote Sens. Environ., 11, 221–229, 1981.

Finizola, A., Sortino, F., Lénat, J.-F., Aubert, M., Ripepe, M., and Valenza, M.: The summit hydrothermal system of Stromboli. New insights from self-potential, temperature, CO_2 and fumarolic fluid measurements, with structural and monitoring implications, B. Volcanol., 65, 486–504, 2003.

Galanopoulos, D. and Kolettis, G.: Investigating the formation of a superficial fracture on Nisyros Island, Greece with the DC resistivity method, Dev. Volcano., 7, 227–240, 2005.

Ganas, A., Lagios, E., Petropoulos, G., and Psiloglou, B.: Thermal imaging of Nisyros volcano (Aegean Sea) using ASTER data: estimation of radiative heat flux, Int. J. Remote Sens., 31, 4033–4047, 2010.

Geshi, N., Acocella, V., and Ruch, J.: From structure- to erosion-controlled subsiding calderas: evidence thresholds and mechanics, B. Volcanol., 74, 1553–1567, 2012.

Gottsmann, J., Rymer, H., and Wooller, L.: On the interpretation of gravity variations in the presence of active hydrothermal systems: insights from the Nisyros Caldera, Greece, Geophys. Res. Lett., 32, L23310, doi:10.1029/2005GL024061, 2005.

Gottsmann, J., Carniel, R., Coppo, N., Wooller, L., Hautmann, S., and Rymer, H.: Oscillations in hydrothermal systems as a source of periodic unrest at caldera volcanoes: multiparameter insights from Nisyros, Greece, Geophys. Res. Lett., 34, L07307, doi:10.1029/2007GL029594, 2007.

Hardee, H.: Permeable convection above magma bodies, Tectonophysics, 84, 179–195, 1982.

Harris, A. and Maciejewski, A.: Thermal surveys of the Vulcano Fossa fumarole field 1994–1999: evidence for fumarole migration and sealing, J. Volcanol. Geoth. Res., 102, 119–147, 2000.

Harris, A., Alparone, S., Bonforte, A., Dehn, J., Gambino, S., Lodato, L., and Spampinato, L.: Vent temperature trends at the Vulcano Fossa fumarole field: the role of permeability, B. Volcanol., 74, 1293–1311, 2012.

Harris, A. J., Lodato, L., Dehn, J., and Spampinato, L.: Thermal characterization of the Vulcano fumarole field, B. Volcanol., 71, 441–458, 2009.

Kinvig, H. S., Winson, A., and Gottsmann, J.: Analysis of volcanic threat from Nisyros Island, Greece, with implications for aviation and population exposure, Nat. Hazards Earth Syst. Sci., 10, 1101–1113, doi:10.5194/nhess-10-1101-2010, 2010.

Lagios, E., Vassilopoulou, S., Sakkas, V., Dietrich, V., Damiata, B., and Ganas, A.: Testing satellite and ground thermal imaging of low-temperature fumarolic fields: the dormant Nisyros Volcano (Greece), Int. Soc. Photogramme., 62, 447–460, 2007.

Lambe, T. W. and Whitman, R. V.: Soil Mechanics SI Version, John Wiley & Sons., 2008.

Marini, L., Principe, C., Chiodini, G., Cioni, R., Fytikas, M., and Marinelli, G.: Hydrothermal eruptions of Nisyros (Dodecanese, Greece): past events and present hazard, J. Volcanol. Geoth. Res., 56, 71–94, 1993.

Matsushima, N., Kazahaya, K., Saito, G., and Shinohara, H.: Mass and heat flux of volcanic gas discharging from the summit crater of Iwodake volcano, Satsuma-Iwojima, Japan, during 1996–1999, J. Volcanol. Geoth. Res., 126, 285–301, 2003.

Mongillo, M. and Wood, C.: Thermal infrared mapping of White Island volcano, New Zealand, J. Volcanol. Geoth. Res., 69, 59–71, 1995.

Nakada, S., Matsushima, T., Yoshimoto, M., Sugimoto, T., Kato, T., Watanabe, T., Chong, R., and Camacho, J. T.: Geological aspects of the 2003–2004 eruption of Anatahan Volcano, Northern Mariana Islands, J. Volcanol. Geoth. Res., 146, 226–240, 2005.

Odong, J.: Evaluation of empirical formulae for determination of hydraulic conductivity based on grain-size analysis, J. Am. Sci., 3, 54–60, 2007.

Papadopoulos, G. A., Sachpazi, M., Panopoulou, G., and Stavrakakis, G.: The volcanoseismic crisis of 1996–97 in Nisyros, SE Aegean Sea, Greece, Terra Nova, 10, 151–154, 1998.

Peltier, A., Finizola, A., Douillet, G. A., Brothelande, E., and Garaebiti, E.: Structure of an active volcano associated with a resurgent block inferred from thermal mapping: the Yasur–Yenkahe volcanic complex (Vanuatu), J. Volcanol. Geoth. Res., 243–244, 59–68, 2012.

Revil, A., Finizola, A., Piscitelli, S., Rizzo, E., Ricci, T., Crespy, A., Angeletti, B., Balasco, M., Barde Cabusson, S., Bennati, L., Bolève, A., Byrdina, S., Carzaniga, N., Di Gangi, F., Morin, J., Perrone, A., Rossi, M., Roulleau, E., and Suski, B.: Inner structure of La Fossa di Vulcano (Vulcano Island, southern Tyrrhenian Sea, Italy) revealed by high-resolution electric resistivity tomography coupled with self-potential, temperature, and CO_2 diffuse degassing measurements, J. Geophys. Res., 113, B07207, doi:10.1029/2007JB005394, 2008.

Sachpazi, M., Kontoes, C., Voulgaris, N., Laigle, M., Vougioukalakis, G., Sikioti, O., Stavrakakis, G., Baskoutas, J., Kalogeras, J., and Lepine, J. C.: Seismological and SAR signature of unrest at Nisyros caldera, Greece, J. Volcanol. Geoth. Res., 116, 19–33, 2002.

Sawyer, G. M. and Burton, M. R.: Effects of a volcanic plume on thermal imaging data, Geophys. Res. Lett., 33, L14311, doi:10.1029/2005GL025320, 2006.

Schöpa, A., Pantaleo, M., and Walter, T.: Scale-dependent location of hydrothermal vents: stress field models and infrared field observations on the Fossa Cone, Vulcano Island, Italy, J. Volcanol. Geoth. Res., 203, 133–145, 2011.

Sekioka, M. and Yuhara, K.: Heat flux estimation in geothermal areas based on the heat balance of the ground surface, J. Geophys. Res., 79, 2053–2058, 1974.

Shepherd, R. G.: Correlations of permeability and grain size, Groundwater, 27, 633–638, 1989.

Shinohara, H., Kazahaya, K., Saito, G., Matsushima, N., and Kawanabe, Y.: Degassing activity from Iwodake rhyolitic cone, Satsuma-Iwojima volcano, Japan: formation of a new degassing vent, 1990–1999, Earth Planets Space, 54, 175–186, 2002.

Springer, D., Loaiciga, H., Cullen, S., and Everett, L.: Air permeability of porous materials under controlled laboratory conditions, Groundwater, 36, 558–565, 1998.

Stacey, T. R., Xianbin, Y., Armstrong, R., and Keyter, G. J.: New slope stability considerations for deep open pit mines, J. S. Afr. I. Min. Metall., 103, 373–390, 2003.

Stevenson, D. S.: Physical models of fumarolic flow, J. Volcanol. Geoth. Res., 57, 139–156, 1993.

Stevenson, J. A. and Varley, N.: Fumarole monitoring with a handheld infrared camera: Volcán de Colima, Mexico, 2006–2007, J. Volcanol. Geoth. Res., 177, 911–924, 2008.

Teschner, M., Vougioukalakis, G., Faber, E., Poggenburg, J., and Hatziyannis, G.: Real time monitoring of gas-geochemical parameters in Nisyros fumaroles, Dev. Volcano., 7, 247–254, 2005.

Teschner, M., Faber, E., Poggenburg, J., Vougioukalakis, G. E., and Hatziyannis, G.: Continuous, direct gas-geochemical monitoring in hydrothermal vents: installation and long-term operation on Nisyros Island (Greece), Pure Appl. Geophys., 164, 2549–2571, 2007.

Tibaldi, A., Pasquarè, F., Papanikolaou, D., and Nomikou, P.: Tectonics of Nisyros Island, Greece, by field and offshore data, and analogue modelling, J. Struct. Geol., 30, 1489–1506, 2008.

Varley, N. R. and Taran, Y.: Degassing processes of Popocatepetl and Volcan de Colima, Mexico, Geol. Soc. Spec. Pub., 213, 263–280, 2003.

Vougioukalakis, G. and Fytikas, M.: Volcanic hazards in the Aegean area, relative risk evaluation, monitoring and present state of the active volcanic centers, Dev. Volcano., 7, 161–183, 2005.

Walter, T. R., Legrand, D., Granados, H. D., Reyes, G., and Arámbula, R.: Volcanic eruption monitoring by thermal image correlation: pixel offsets show episodic dome growth of the Colima volcano, J. Geophys. Res.-Sol. Ea., 118, 1408–1419, 2013.

Yudovskaya, M. A., Tessalina, S., Distler, V. V., Chaplygin, I. V., Chugaev, A. V., and Dikov, Y. P.: Behavior of highly-siderophile elements during magma degassing: a case study at the Kudryavy volcano, Chem. Geol., 248, 318–341, 2008.

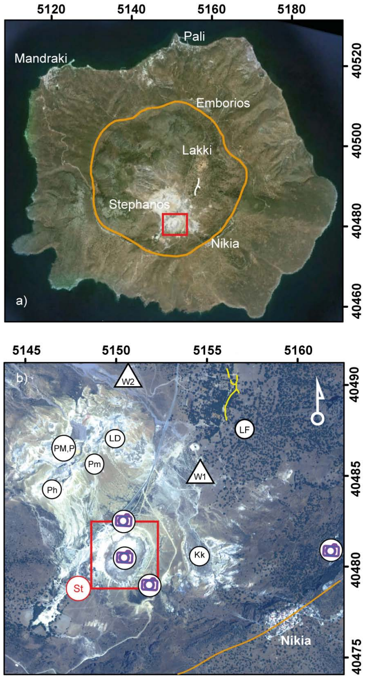

Fig. 1. (a) Nisyros island, coordinates are in UTM, zone 35, grid ticks are at 2 km. The brown line marks the border of the caldera. Inside the caldera: the red square shows the position of Stefanos craters; the white line highlights the 2001–2002 fissure at the Lakki plain. Other toponyms outside the caldera indicate the villages on the island. **(b)** Satellite image (WV02) showing the main volcanic features inside the caldera; grid ticks are at 500 m. The red square indicates the Stefanos crater labeled (ST); other labeled sites are the Kaminakia crater (Kk), the Lofos dome (LD), the nested Polybotes Megalos and Polybotes craters (PM, P), Polybotes Micro crater (Pm) and Phlegeton crater (Ph). LF is the fissure in the Lakki plain. The camera icons point the position where IR and OP images were collected, inside-outside of Stefanos crater and at the caldera border (brown line).

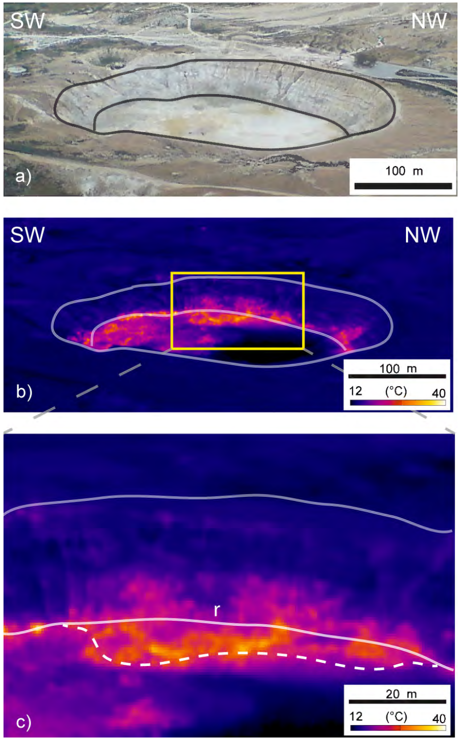

Fig. 2. (a, b) OP and IR images collected from long distance (caldera rim, Fig. 1b). Solid lines mark the upper and lower crater rim. Both the OP and IR images display part of the crater floor and the east-facing flank; the IR images show thermal anomalies along the bottom rim and a weaker anomaly toward the center of the crater but also propagating to the south. The yellow rectangle in **(b)** defines the area shown by the close-up in **(c)**. **(c)** Magnification of the wide thermal anomaly (r, dashed line) on the western side of the crater. The coarse spatial resolution (∼ 0.7 m) causes the smoothed appearance of the temperatures.

Title Page
Abstract Introduction
Conclusions References
Tables Figures
|◀ ▶|
◀ ▶
Back Close
Full Screen / Esc
Printer-friendly Version
Interactive Discussion

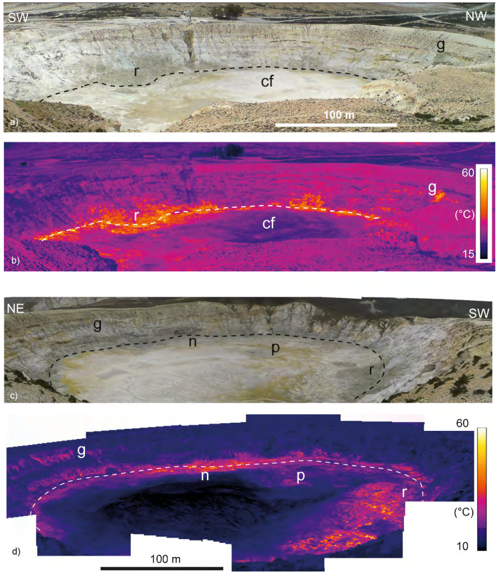

Fig. 3. (a, b) OP and IR daytime panorama viewing westward; the dashed line marks the crater's bottom rim. **(b)** The thermal anomaly is visible at the break in slope of the flank and is wider in correspondence to the mound (r). The crater floor (cf) and the flank are generally cold; the lateral thermal gradient (form SW to NW) on the flank appears because of the insolation. The thermal anomaly along the flank (g) is volcanic and is stronger than the insolated areas. The insolation and the fine spatial resolution allow the IR data to display morphological features (e.g. horizontal layering gullies). Temperature values are saturated at 15 and 60 °C to optimize the view. c, d) OP and IR nighttime panorama facing southeastward; the dashed line marks the crater bottom rim. **(d)** The thermal anomaly clearly shows its ring-shaped pattern at the break in slope of the flank, at the eastern (n) and western (r) sides the anomaly appears to be wider. Another anomaly (p) appears close to the center in the south direction and represents the mud pits. Also visible is the thermal anomaly (g) along the flank, as observed in **(c, d)**. Temperature values are saturated at 10 and 60 °C to optimize the view. **(a, c)** Show also the sites with high sulfur content (yellowish).

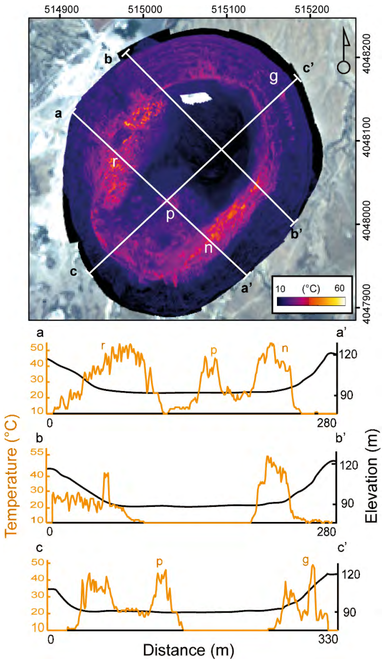

Fig. 4. (Above) Georeferenced IR mosaic showing the full extent of the ring-shaped thermal field along the bottom crater rim. Grid ticks are at 100 m. This map better highlights the NW–SE trending of the wider anomalies including the mounds (r, n) as well as the isolated position of the boiling ponds (p) and of the anomaly along the northern flank (g). Temperature values are saturated at 10 and 60 °C to optimize the view. Three orthogonal traces (*a*–*a*′, *b*–*b*′, *c*–*c*′) are shown intersecting those features. (below) Temperature-topography profiles (*a*–*a*′, *b*–*b*′, *c*–*c*′); the distances along the trace and the topographic height (x–y axis are not scaled) are in black; the temperature axis and the values are in orange. These profiles highlight that thermal anomalies occur mostly at breaks in the slope.

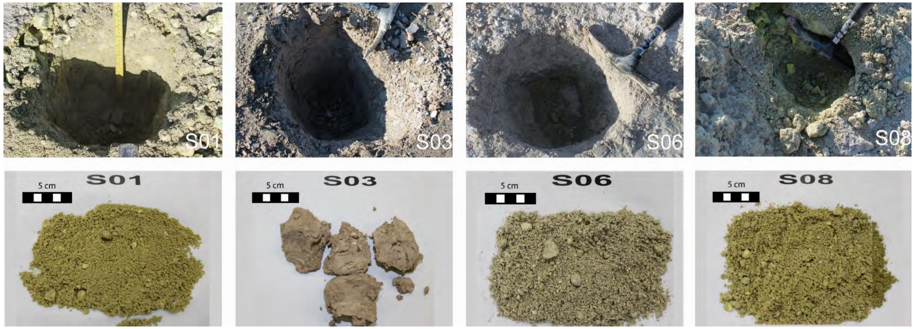

Fig. 5. (Left) Digital pictures of the pits where soil samples were collected and (right) corresponding material. The difference between granular and cohesive types can be distinguished visually. S01 is loose and shows few clasts ≥ 1 cm dispersed in ∼ uniform fine sand matrix. S03 occurs in blocks of cohesive material and no particle can be distinguished. S06 is loose and shows few clasts ≥ 1 cm, but the matrix is graded. S08 has few clasts ≥ 1 cm and appears graded. S01 and S06 have also sulfur grains as indicated by the yellowish color respect to the grayish S06.

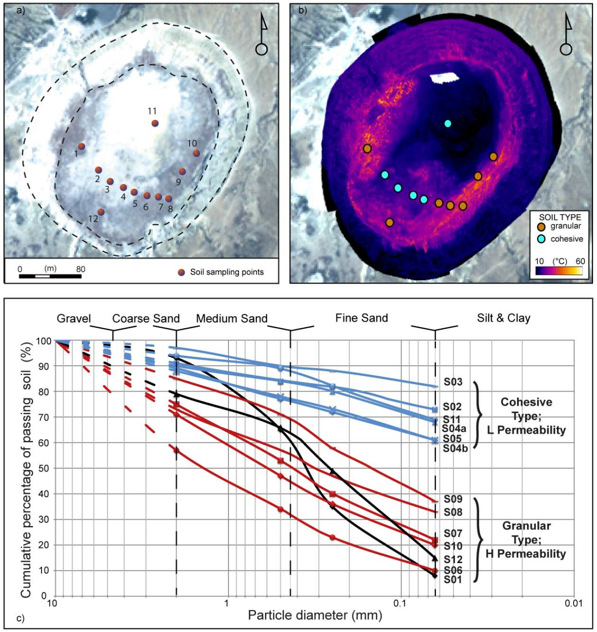

Fig. 6. (a) Optical satellite image (WV02) of the Stefanos crater: the numbered dots mark the sites where soil was sampled. **(b)** Georeferenced IR mosaic overlapping the satellite images; it shows the coupling of soil types with the thermal field. **(c)** Semi-logarithmic plot of grain-size curve. The vertical axis indicates the cumulative percentage (by weight) of material passing through the sieves; the lower horizontal axis indicates the mesh diameter of the sieves. The upper horizontal axis indicates the fraction names and intervals according to international standards. The blue lines are the grain-size curves of cohesive type soils, which have low (L) permeability. The red and black lines indicate the grain-size curves of granular type soils, which have high (H) permeability. The red curves are for sorted samples, the black for more uniform samples. Blue, red and black lines are solid within the measured intervals and dashed where uncertainty arises by assuming a maximum diameter of 10 mm and interpolating the curve (see text).

Title Page
Abstract
Introduction
Conclusions
References
Tables
Figures
◀|
|▶
◀
▶
Back
Close
Full Screen / Esc
Printer-friendly Version
Interactive Discussion

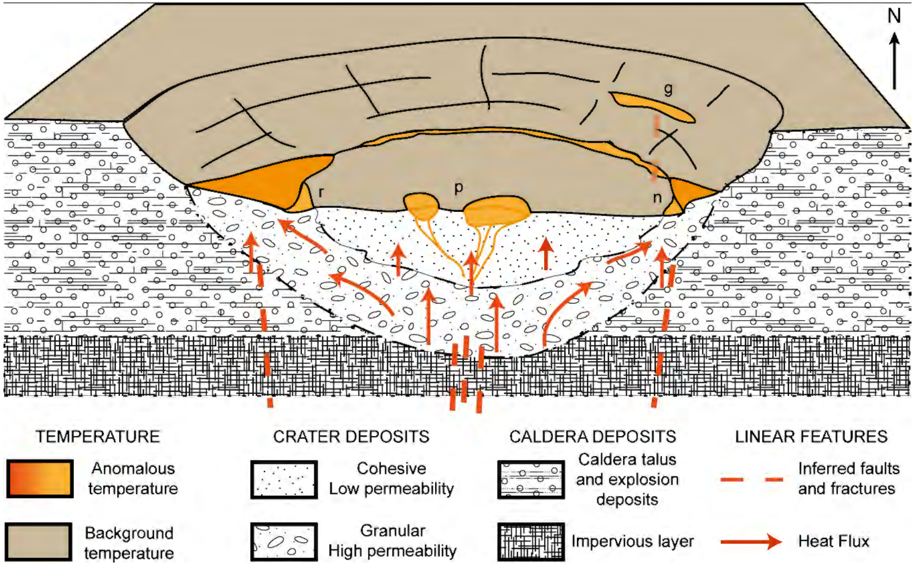

Fig. 7. Sketch (not to scale) of the conceptual model. At the bottom an impervious layer is broken by faults which drive the phreatic explosion through the caldera talus and the deposits of an older eruption. On top of the impervious layer is the crater. The heat rising from the depths enters the crater through the faults and propagates upward. According to our hypothesis, the crater is initially filled by granular and permeable deposits that progressively appear only at the sides. Later cohesive and impermeable material deposits on top and in heteropy to the coarse ones. The heat flux rises with different efficiency: high in granular deposits (longer arrows), low in cohesive deposits (shorter arrows). Because of the low permeability at the crater center, fluids are forced to move sideways increasing the degassing at the border. Possibly there are also other sideways faults which enhance the heat release at the NW and SE sites (r, n) and funnel hot fluids higher along the NE flank (g). Fault(s) at the crater center are also responsible for drainage and erosion of the crater filling, by which finally mud pits generate (p). At the surface, the thermal anomalies are presented in light and dark orange to indicate temperature differences. Brown is the cool terrain corresponding to the background temperature.

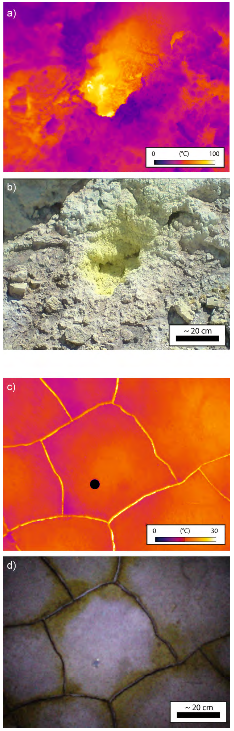

Fig. 8. (a, b) IR and OP close-ups of a fumarole on the western mound. The IR image shows that the temperature at the vent reaches 100 °C, according to direct measurements. This is possible as the pixel size is sub-mm. It also shows that *T* rapidly decreases sideway. The same can be deduced by the OP where solid sulfur exists close to the degassing vent. **(c, d)** IR and OP close-up of dessication polygon. The IR image shows the plate as cool whereas the bounding fracture is ~ 5 °C warmer. The black circle is 1 Euro coin for scale; it results cooler because it has an emissivity different from the emissivity of the soil. The OP image shows the sulfur crystallization close to the fracture.

Title Page
Abstract | Introduction
Conclusions | References
Tables | Figures
|◀ | ▶|
◀ | ▶
Back | Close
Full Screen / Esc
Printer-friendly Version
Interactive Discussion